Low-field NMR relaxation analysis of high-pressure ethane adsorption in mesoporous silicas

Kaishuo Yang, Ehsan S. Pouya, Libin Liu, Ming Li, Xiaoxian Yang, Neil Robinson, Eric F. May and Michael L. Johns*

Department of Chemical Engineering, The University of Western Australia, 35 Stirling Highway, Perth, WA 6009, Australia

***Corresponding Author:**
Prof Michael L. Johns
Chair of Chemical and Process Engineering
The University of Western Australia

Postal Address:
Department of Chemical Engineering
The University of Western Australia
35 Stirling Highway (M050)
Perth WA 6009
Australia

Phone: +61 (08) 6488 5664
Email: michael.johns@uwa.edu.au
Fluid Science and Resources Research Group: www.fsr.ecm.uwa.edu.au

Author ORCID:

Kaishuo Yang	0000-0001-8544-9955
Ehsan S. Pouya	0000-0001-6389-2964
Libin Liu	0000-0002-5387-7098
Ming Li	0000-0001-9861-7858
Xiaoxian Yang	0000-0003-4655-3156
Neil Robinson	0000-0002-0893-2190
Eric F. May	0000-0001-5472-6921
Michael L. Johns	0000-0001-7953-0597

Abstract

Understanding the behaviour of short-chain hydrocarbons confined to porous solids informs the targeted extraction of natural resources from geological features, and underpins rational developments in separation, storage and catalytic conversion processes. Here we report the application of low-field (12.7 MHz) ^{1}H nuclear magnetic resonance (NMR) relaxation measurements to characterise ethane dynamics within mesoporous silica materials exhibiting mean pore diameters between 6 and 50 nm. Our measurements provide NMR-based adsorption isotherms within the range 25-50 bar and at ambient temperature, incorporating the ethane condensation point (40.7 bar at our experimental temperature of 23.6 °C). The quantitative nature of the acquired data is validated via a direct comparison of NMR-derived excess adsorption capacities with ex situ gravimetric ethane adsorption measurements, which are demonstrated to agree to within 0.2 mmol/g of the observed ethane capacity. NMR T_2 relaxation time distributions are further demonstrated as a means to decouple interparticle and mesopore dominated adsorption phenomena, with unexpectedly rapid relaxation rates associated with interparticle ethane gas confirmed via a direct comparison with NMR self-diffusion analysis.

Keywords:

adsorption; condensation; mesoporous materials; nuclear magnetic resonance; NMR relaxation

Table of contents text and image

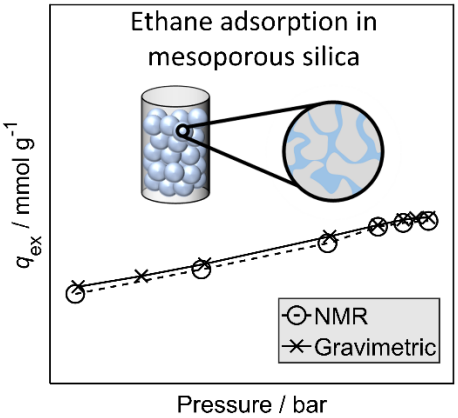

We demonstrate simple low-field (12.7 MHz) ^{1}H NMR relaxation measurements as a quantitative tool with which to inform high-pressure hydrocarbon gas adsorption and liquefaction phenomena within a range of high surface area mesoporous silica materials with pore sizes between 6 nm and 50 nm.

1. Introduction

Mesoporous materials (exhibiting pore structures 2-50 nm in diameter) find widespread applications across separation, storage and catalytic processes, wherein their efficacy is conferred by inherently large surface-to-volume ratios and high degrees of pore surface accessibility[1]. Understanding the adsorption and uptake of gaseous hydrocarbons within such materials underpins their rational design for the upgrading of chemical feedstocks[2,3], and provides well-defined model systems with which to inform the extraction of resources from natural hydrocarbon reserves, such as shale formations[4]. Oxide-based materials, including silicas (SiO_2), aluminas (Al_2O_3) and titanias (TiO_2), offer ubiquitous and tuneable mesoporous frameworks for such applications[5]. For instance, metal oxides are known to provide a range of active pore surface properties including photoactive centres[6] and catalytic acid and base sites[7,8], while silica-based materials, including gels and colloidally-templated frameworks, provide inert substrates with highly controllable pore topologies[9–11].

Traditional approaches to characterise gas uptake phenomena within mesoporous materials are based on gravimetric or volumetric measurements. Such methods are established across a range of pressure and temperature conditions[12–14], providing quantitative routes to molecular uptake data, and via the application of well-established models facilitate the characterisation of material properties including pore size distributions and accessible surface areas[15]. However, drawbacks of such analyses include long experimental time scales (hours-to-days) and the requirement for access to specialist sorption hardware. Here we explore alternative routes to hydrocarbon gas uptake data via the application of time-domain nuclear magnetic resonance (NMR) measurements. NMR spectroscopy is a universally applied characterisation technique for establishing molecular and solid-state structures; however, in the case of fluids confined to mesoporous materials the insight available from such frequency-domain chemical shift data is usually limited by significant line-broadening effects[16], which occur as a result of local magnetic field distortions due to magnetic susceptibility differences across the solid-fluid interface[17]. Time-domain NMR measurements instead probe the decay rates of observable NMR signals as a result of molecular dynamics, and are broadly immune to such magnetic field distortions. NMR relaxation measurements probe the longitudinal and/or transverse relaxation behaviour of the spin system under investigation, as characterised by the time constants T_1 and T_2, respectively. These time constants exhibit well-defined relationships with molecular rotational and translational dynamics within the unrestricted bulk liquid phase[18]. For fluids confined to porous solids, however, the correspondence between time constants and molecular dynamics is perturbed by the attendant pore structure[19,20], facilitating characterisation of a range of material and interfacial properties including pore sizes[21,22] and connectivity[23–25], surface areas[26,27], confinement effects[28–30] and adsorption interactions[31–37]. Papaioannou *et al.*[38] recently employed a range of high-field NMR relaxation measurements to investigate methane storage within mesoporous (5.7 nm diameter pores) Vycor glass (silica) at 7 – 897 bar, demonstrating the sensitivity of such measurements to both monolayer and multilayer adsorption phenomena. Alternatively,

pulsed field gradient (PFG) NMR diffusion measurements apply a series of short magnetic field gradient pulses to track the diffusive displacement of NMR-active species across a set observation period[39]. PFG NMR diffusion measurements have been applied to a wide range of fluids confined within mesoporous solids, facilitating the elucidation of restricted mass transport phenomena[40] and surface dynamics[41–43], together with material characteristics including pore structure tortuosity values[44–46] and pore isotropies[47–49]. High-field PFG NMR measurements have been reported for the characterisation of short-chain hydrocarbon gas dynamics within a range of templated mesoporous silica materials[50–52].

In the present work we demonstrate the utility of low magnetic field NMR relaxation and diffusion measurements for the characterisation of hydrocarbon gas dynamics within mesoporous silica materials. Low-field NMR experiments utilise benchtop instruments equipped with permanent magnet-based hardware[53–55], and provide a number of advantages over classical high-field superconducting NMR equipment, including increased portability, reduced safety considerations and negligible maintenance requirements; such characteristics lend low-field NMR equipment to straightforward integration with high-pressure apparatus[56–58]. Low-field experimentation is further advantageous in the characterisation of T_2 transverse relaxation processes, wherein reduced magnetic field strengths limit undesirable magnetic susceptibility contrast effects at the solid/fluid interfaces, which result in enhanced rates of transverse relaxation[17]. Low-field relaxation and diffusion measurements have been reported for methane within a variety of microporous solids including carbons[59,60], zeolites[61], MOFs[59], while direct integration with volumetric sorption hardware has also been demonstrated in the case of vapour phase alcohols[62]. Here, we extend this field through the investigation of ethane sorption within a range of mesoporous silicas exhibiting a well-defined range of mean pore diameters (6, 15 and 50 nm). Our measurements are performed across the pressure range 25-50 bar, which at room temperature incorporates the condensation point of bulk ethane, and detail direct comparisons between time-domain NMR measurements and conventional gravimetric sorption analysis.

2. Theoretical background

Adsorption and capillary condensation

Adsorption processes involve the thermodynamically favourable adhesion of chemical species to solid surfaces[63]. For hydrocarbon gases in the vicinity of oxide surfaces such interactions occur via a non-dissociative physisorption mechanism[15], which increases the molecular density of the adsorbed surface layer to near that of the condensed bulk phase. Capillary condensation then describes the phenomenon whereby the multilayer adsorption of confined gas leads to condensation at pressures below the bulk saturation pressure of the imbibed fluid[64]. This process is quantified by way of the Kelvin equation[65], which takes the form[66]

$$P_{\mathrm{vap}} = P_{\mathrm{sat}} \exp\left(\frac{-2\gamma_l V_l \cos\theta}{rRT}\right). \quad (1)$$

Here P_{vap} is the vapour pressure at which capillary condensation emerges, P_{sat} is the bulk saturation pressure, γ_l are V_l are the surface tension and molar volume of the adsorbed liquid, respectively, θ is the contact angle, r is the mean pore radius, R is the gas constant and T is the absolute temperature.

NMR relaxation and diffusion in porous media

In this work we focus on the transverse ^{1}H (proton) relaxation behaviour of free and confined ethane, as characterised by the time constant T_2. Nuclear spin relaxation processes exhibit well-defined relationships with the translational and rotational dynamics of spin-bearing molecules. For unrestricted (bulk) gases such relaxation processes are dominated by the so-called spin-rotation relaxation mechanism[67–69], while dipolar relaxation processes dominate within the condensed phase[18], including molecular layers formed upon adsorption[70]. For short-chain hydrocarbon fluids confined to mesoporous materials, the observed relaxation characteristics are dominated by rapid exchange across the pore structure, described as a weighted averaged of contributions from both adsorbed species at the solid/fluid interface and bulk-like fluid towards the centre of the pores. The resulting relaxation rates may be expressed as[71]

$$\frac{1}{T_2} = \frac{1-P}{T_{2,\mathrm{bulk}}} + \frac{P}{T_{2,\mathrm{ads}}}. \quad (2)$$

Here, T_2 is the observed relaxation time constant, $T_{2,\mathrm{bulk}}$ is the time constant for the unrestricted fluid, while $T_{2,\mathrm{ads}}$ is the time constant for species adsorbed at the pore surface. The term P describes the fraction of spins within the adsorbed surface layer, with $1-P$ spins occupying the bulk-like centre of the pore. This term may be further expanded as $P = \lambda S/V$, where S/V describes the accessible surface-to-volume ratio of the confining pore structures, while λ defines the thickness of the adsorbed surface layer. As this length scale is typically small relative to the pore radius, **Equation (2)** may be further expressed as[70]

$$\frac{1}{T_2} \approx \frac{1}{T_{2,\mathrm{bulk}}} + \rho_2 \frac{S}{V}, \tag{3}$$

where $\rho_2 = \lambda / T_{2,ads}$ defines the transverse surface relaxivity; given the general case that $T_{2,bulk} > T_{2,ads}$, this term then provides an approximate scaling factor between observed relaxation characteristics and pore size.

The self-diffusion characteristics of confined hydrocarbons are also perturbed through repeated interactions with the pore walls of the adsorbing solid, reducing the bulk self-diffusion coefficient D_0 to an effective self-diffusion coefficient D_{eff}. The relationship between D_0 and D_{eff} is strongly dependent on both the structure of the confining pore network and the observation period employed, with differing degrees of observed diffusive restriction characterised by the parameter[39]

$$\xi = \frac{D_0 \Delta}{r^2}, \tag{4}$$

where Δ is the observation period and r is the pore radius. Short-, intermediate- and long-time diffusion limits are characterised by ξ values $\ll 1$, ~ 1 and $\gg 1$, respectively, and are described in detail elsewhere[39]. Here we focus on diffusive characteristics which obey the long-time diffusion limit, where the effective self-diffusion coefficient D_{eff} is reduced from that of the unrestricted fluid according to[72]

$$D_{eff} = \frac{D_0}{\tilde{\tau}}, \tag{5}$$

with $\tilde{\tau}$ representing the pore network tortuosity.

3. Experimental

Materials

Mesoporous CARiACT Q-series silica gel materials were obtained from Fuji Silysia Chemical Ltd (Japan). The silicas comprised spherical particles ranging in diameter between approximately 2 mm and 5 mm (particle size distributions are provided in **Figure S1** of the **Supplementary Information**) and exhibited nominal mean pore diameters of 6, 15 and 50 nm; these materials are referred to as Q6, Q15 and Q50, respectively. Ethane (purity > 99.99 %) was obtained from Coregas (Australia).

Material characterisation

Silica pore size distributions, together with specific surface area and cumulation pore volume values, were measured via the acquisition of nitrogen isotherm data at 77 K using a Micromeritics ASAP 2020 adsorption analyser. Prior to each measurement approximately 0.5 g of each material was heated for 10 hours at 200 °C under vacuum to remove any physisorbed water. Barrett-Joyner-Halenda (BJH) pore size distributions were obtained from the desorption branch of each isotherm and are detailed in **Figure 1**, while Brunauer-Emmett-Teller (BET) surface areas were calculated from each adsorption branch within the relative pressure range 0.05 – 0.35. **Table 1** provides a summary of the physical properties of the Q-series silica gels.

Table 1. Material physical properties of mesoporous CARiACT Q6, Q15 and Q50 silicas.

	Q6	Q15	Q50
Modal pore diameter / nm	6.0	14.9	52.6
Specific surface area / $m^2\ g^{-1}$	386	206	72
Cumulative mesopore volume / $cm^3\ g^{-1}$	0.54	0.90	0.91
Surface area-to-volume ratio / m^{-1}	7.15×10^8	2.29×10^8	7.91×10^7

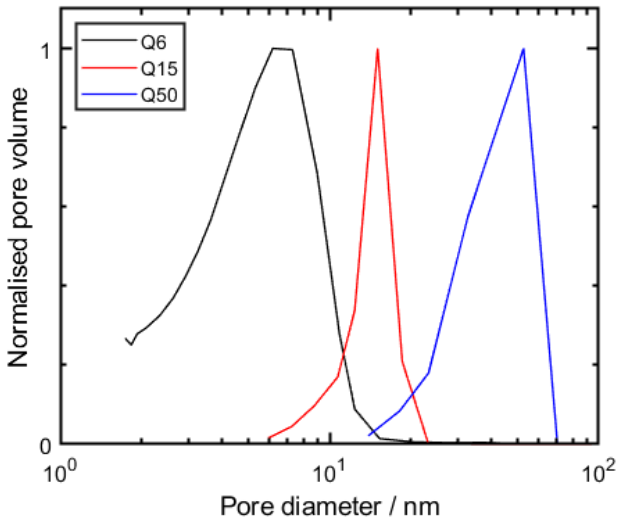

Figure 1. BJH pore size distributions of mesoporous CARiACT Q6, Q15 and Q50 silicas.

NMR measurements

Ethane NMR measurements were performed using an Oxford Instruments Geospec spectrometer equipped with a 0.3 T parallel plate magnet array (corresponding to a ^{1}H NMR frequency of ν_0 = 12.7 MHz) and high pressure P5 overburden cell (Green Imagine Technologies). A schematic of the experimental setup used here is shown in **Figure 2**: A cylindrical PEEK (polyether ether ketone) cell (inner diameter = 18 mm, outer diameter = 25 mm, length = 45 mm) was used to hold the silica particles and was wrapped with FEP heat shrink tubing to secure the holder between two PEEK gas distribution plugs. Two syringe pumps (Teledyne ISCO 260D) were employed in constant pressure mode to apply both ethane and a ^{1}H NMR-silent fluorinated confining oil (Fluorinert FC-40) to the system; the latter was set to provide a 50 bar differential pressure above the sample pressure so as to seal the sample cell in place. A vacuum pump (Agilent Technologies DS-102) was used to degas the silica materials and associated experimental apparatus for at least 12 hours before pressurisation with ethane. Pressures were then monitored and recorded using two pressure transducers (Swagelok S model), while pump volume and flow rate data were monitored using LabView (National Instruments Cooperation, USA). Fluid temperatures within the magnet bore were maintained at 23.6 ± 0.2 °C via integration of the syringe pumps with a heated water bath, with the system temperature monitored and recorded via a calibrated temperature sensor.

Prior to our NMR analysis each silica material was dried in air at 120 °C for at least eight hours. Transverse relaxation data were acquired by applying the standard CPMG (Carr-Purcell-Meiboom-Gill) pulse sequence shown in **Figure 3a**[73,74]. Following initial polarisation along the direction of the static magnetic field (conventionally the *z*-direction) a 90° radio frequency (RF) pulse excites the spin system into the *xy*-plane, where it undergoes transverse relaxation. A series of n 180° refocussing RF pulses are then applied to counter dephasing due to inhomogeneities within the static field, inducing a train of n spin echoes which decay according to T_2. Each spin echo magnitude $S(nt_e)$ was recorded as a single data point (white data point within **Figure 3a**). In this work the echo time was set to $t_e = 250$ μs while up to $n = 40{,}000$ echoes were acquired to ensure the CPMG data decayed to the noise floor.

Diffusion data were acquired by applying the pulsed gradient stimulated echo (PGSTE) sequence shown in **Figure 3b**[75,76]. Here, once excited in the *xy*-plane by a 90° RF pulse, a magnetic field gradient pulse of strength g and length δ imparts a spatially dependent phase across the spin system, encoding the initial positions of the nuclear spin ensemble. A second 90° pulse returns the spin system to the longitudinal axis for a storage time of length T, during which a homospoil gradient is applied to remove any remaining coherent transverse magnetisation. A third 90° pulse returns the system to the *xy*-plane; here, a second gradient pulse of equal area $g\delta$ is applied to decode the positions of the nuclear spin ensemble, inducing a stimulated echo of magnitude $S(g)$ which attenuates as a function of increasing molecular displacement during the observation period (inter-gradient spacing) $\Delta = \mathrm{T} + \tau$. Our PGSTE measurements were performed holding the gradient

pulse length $\delta = 1.5$ ms and inter-gradient pulse duration $\Delta = 30$ ms constant while varying the gradient strength across 16 linearly spaced values up to a maximum of g = 0.25 T m^{-1}. The inter-90 spacing was $\tau = 5$ ms, while the homospoil gradient was set to 7.65×10^{-4} T m^{-1} and was applied for 1 ms. A total of 4 repeat scans were employed for both CPMG and PGSTE measurements and were separated by a recycle delay of 60 s, providing signal-to-noise ratios >200.

Approximately 5 g of each silica material was employed, with background T_2 measurements performed under vacuum and subtracted from the subsequently acquired ethane data during processing; such background relaxation signals are primarily associated with O-rings within the high-pressure P5 overburden cell. To minimise the influence of gas/liquid phase changes on the acquired data, all experiments were conducted after suitably long equilibration times (approximately 120 minutes) following pressure alterations, such that a constant zero ethane pump flow rate, together with constant NMR signal magnitudes, were recorded.

Supplementary NMR relaxation measurements were also performed on water saturated silica samples. Each silica material was again dried in air at 120 °C for at least eight hours, then saturated with deionised water for at least 48 hours before use. Measurements were again performed using a 12.7 MHz Oxford Geospec spectrometer, in this case equipped with a 53 mm Q-sense probe. Saturated silica materials were placed within a 7 ml glass vial at the centre of the magnet bore, with the height of the interparticle water set to cover the top-most silica spheres within the sample.

NMR data processing

Acquired T_2 data may be described by the Fredholm integral equation[77]

$$\frac{S(nt_e)}{S(0)} = \int \exp\left(\frac{-nt_e}{T_2}\right) F(T_2)\, d\log_{10}(T_2) + \varepsilon(nt_e). \tag{6}$$

Here $S(nt_e)/S(0)$ is the normalised NMR spin echo signal intensity and $\varepsilon(nt_e)$ represents the experimental noise, assumed Gaussian with zero mean; $F(T_2)$ is the targeted distribution of T_2 relaxation times and was acquired via numerical inversion of the acquired CPMG data according to **Equation (6)**. Acquired diffusion data is similarly described by the expression[77,78]

$$\frac{S(g)}{S(0)} = \int \exp\left(-\gamma^2 g^2 \delta^2 \left\{\Delta - \frac{\delta}{3}\right\} D\right) F(D)\, d\log_{10}(D) + \varepsilon(g). \tag{7}$$

Here $S(g)/S(0)$ is the normalised NMR stimulated echo signal intensity, γ is the gyromagnetic ratio of the ^{1}H nucleus, and $\varepsilon(g)$ is the experimental noise; $F(D)$ is the targeted distribution of diffusion coefficient values and was acquired via numerical inversion of the acquired PGSTE data according to **Equation (7)**. Stability of the inverted relaxation and diffusion distributions was enforced via the application of Tikhonov regularisation[79], with the magnitude of the smoothing parameter chosen according to the generalised cross-

validation method[80]. The inversion algorithm was written in MATLAB (MathWorks Inc.) and first used by Griffith *et al.*[81] and Hollingsworth *et al*.[82] for relaxation and diffusion analysis, respectively.

Gravimetric adsorption measurements

Ethane adsorption measurements were performed under identical pressure and temperature conditions as the above NMR measurements using a gravimetric sorption analyser (Rubotherm, Germany; now TA instruments, USA). The measurement cell temperature was detected using a calibrated 100 Ω platinum resistance thermometer, with the thermometer resistance measured using a digital multimeter (Millik Precision Thermometer, Isotech, UK). The cell pressure was measured with a vibrating quartz-crystal-type transmitter (Paroscientific, USA) with a range up to 41.3 MPa. The mass of the porous samples was conducted using an analytical balance via a magnetic suspension coupling; the net adsorbed mass m_{net} on the adsorbent sample is given as[83,84]

$$m_{net} = m^*_{fluid} - m^*_{vac} + \rho_{fluid} V_c. \tag{8}$$

Here, $m^*_{fluid} = (W_1 - W_0)_{fluid}/\alpha$, and $m^*_{vac} = (W_1 - W_0)_{vac}/\alpha$, where W_0 and W_1 are the readings of the magnetic suspension balance at the zero position and measurement position, respectively, $\alpha = (1 - \rho_{air}/\rho_{calib})^{-1} \approx 1.000150$ is the balance calibration factor, with ρ_{air} and ρ_{calib} representing the densities of air in the laboratory and the calibration mass, respectively, while the subscripts "vac" and "fluid" denote that the measurements are conducted with the measurement cell both evacuated and filled with ethane, respectively. In **Equation (8)**, ρ_{fluid} is the density of the fluid, which is calculated using reference equations of state using the measured temperature and pressure, while V_c is the volume of the sample container. For a non-adsorbing fluid (e.g. helium) the volume of the sample skeleton V_s may be calculated according to

$$V_s = -m_{net}/\rho_{fluid}. \tag{9}$$

In practice, however, V_s is regressed as the slope of multiple (ρ_{fluid}, m_{net}) measurements along an isotherm. The excess adsorbed mass m_{ex} is then calculated according to

$$m_{ex} = m_{net} + \rho_{fluid} V_s, \tag{10}$$

with the corresponding adsorption capacity expressed as

$$q_{ex} = \frac{(m_{ex}/M_{fluid})}{m_s}, \tag{11}$$

where M_{fluid} and m_s are the molar mass of the adsorbate investigated and the mass of the adsorbent, respectively.

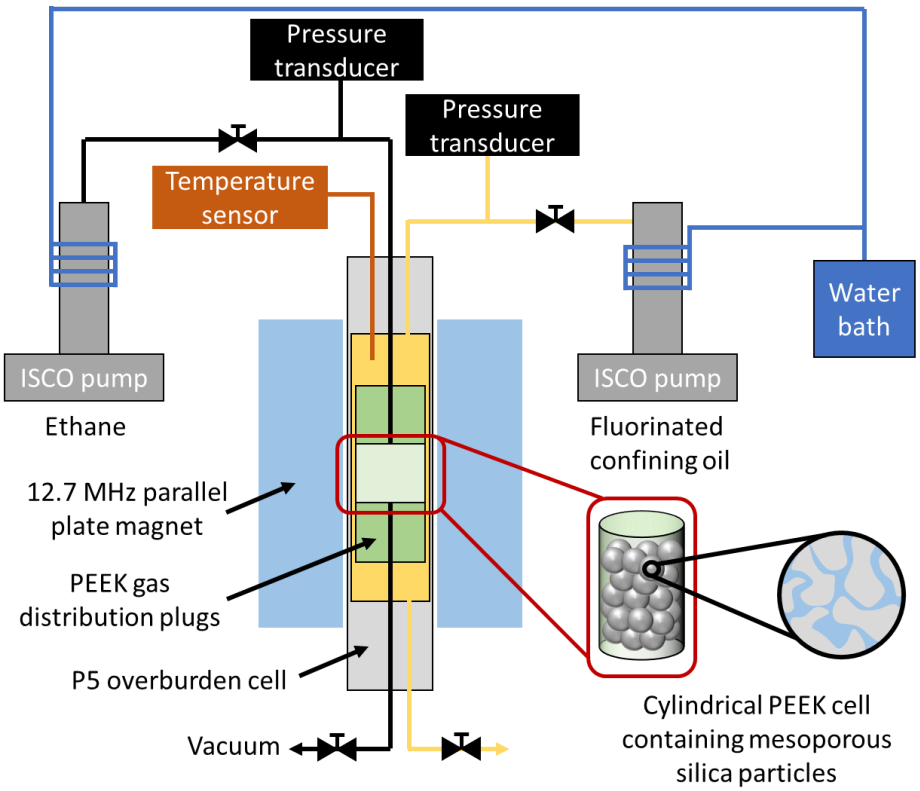

Figure 2. Schematic of the experimental apparatus employed to perform NMR measurements.

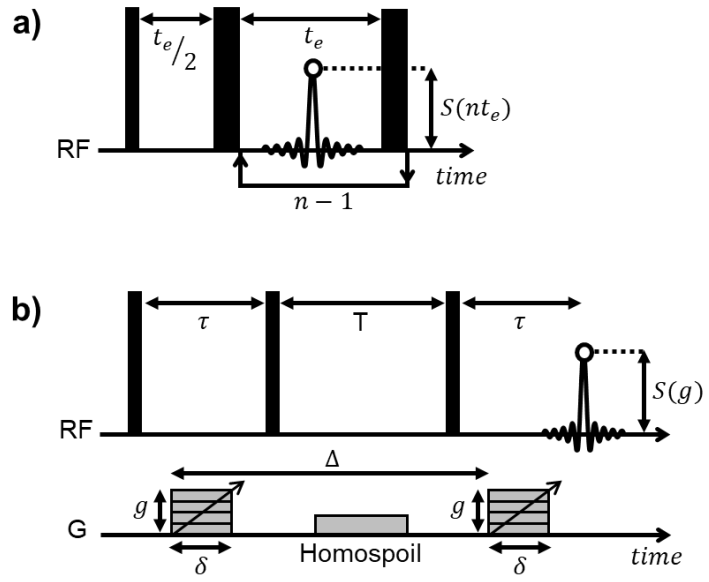

Figure 3. NMR radio frequency (RF) pulse sequence diagram for **a)** CPMG measurements and **b)** PGSTE measurements. Thick and thin bars represent 180° and 90° RF pulses, respectively, while white data points indicate the recorded echo magnitudes. In **b)** gradient pulse timings (G axis) are given according to the notation of Tanner[76]; gradient pulses of incremental magnitude g are illustrated with effective pulse durations δ, while the observation time is Δ. Homospoil gradients are also shown and are applied during the storage period T. The experimental variables t_e and n are discussed within the main text.

4. Results and discussion

Bulk ethane measurements

NMR measurements were first conducted on bulk ethane in the absence of any adsorbents. The signal acquired from the first echo of the acquired CPMG echo train was acquired as a close approximation to NMR signal in the absence of relaxation, and is considered here to represent the total ^{1}H density (and hence ethane density) within the NMR measurement system. **Figure 4a** shows a direct correlation between the evolution of this acquired signal magnitude across the range 30 – 45 bar with bulk ethane saturation pressure values calculated from the reference equation of state by Büecker and Wagner[85], as implemented in the National Institute of Standards and Technology (NIST) Chemistry Web book[86]. A strong linear correlation is apparent, demonstrating the sensitivity of our NMR analysis to increasing ethane density; a simple linear fit (dashed line within **Figure 4a**; $R^2 > 0.999$) then provides a scaling factor between acquired NMR signal magnitudes and the ethane content of our measurement system. **Figure 4b** further illustrates the evolution of ethane density as a function of pressure as calculated with the reference equation of state and by our calibrated NMR signal data. Excellent agreement in observed data behaviour is readily apparent, providing validation of our experimental NMR method. Our acquired NMR signal increases gradually for ethane pressures up to 40.8 bar due to increasing molecular density within the gas phase. A steep signal increase between 40.1 bar and 40.8 bar then indicates the onset of bulk ethane condensation, which occurs in close agreement with the expected bulk saturation pressure of 40.68 bar at 23.6 °C (as obtained from the reference equation of state implemented in the NIST database).

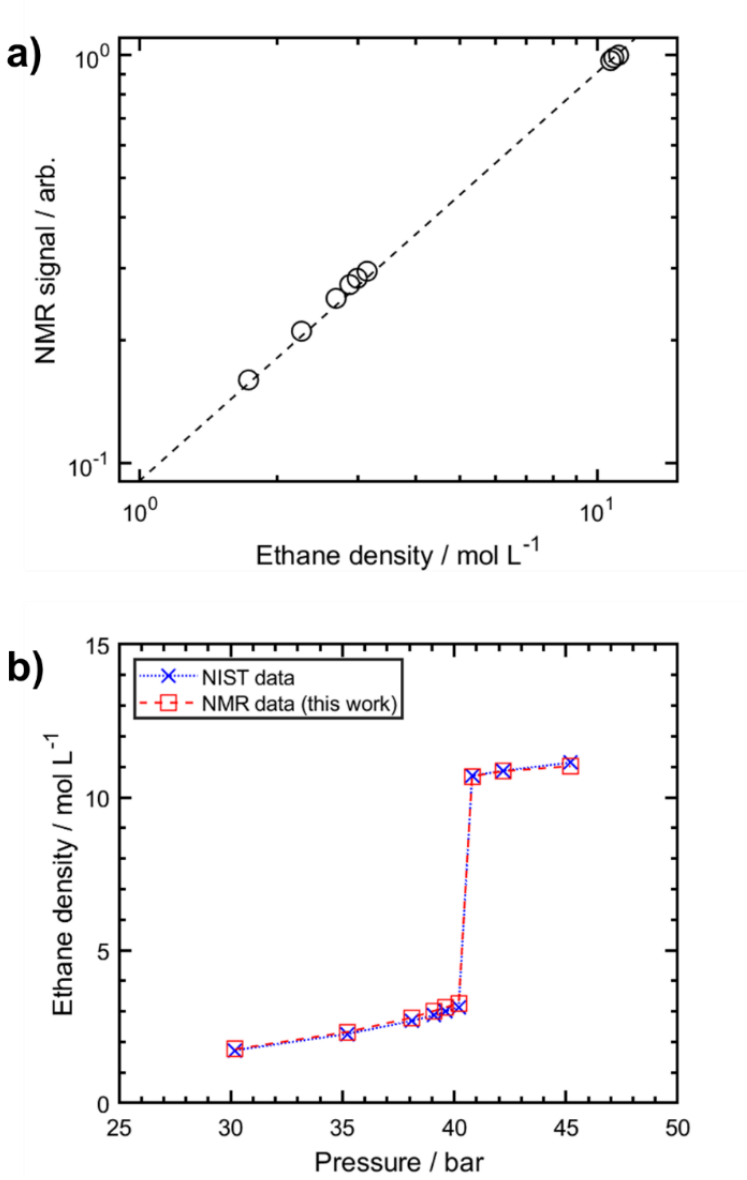

Figure 4. a) Direct correlation of bulk ethane saturation pressure values (obtained from the NIST Web book) with measured NMR signal magnitudes, as approximated from the first echo ($t_e = 250$ µs) of each CPMG echo train; the dashed diagonal line indicates a linear fit to the data, and provides a scaling factor between NMR data and ethane density. **b)** Ethane density evolution as a function of pressure. Calibrated NMR data provides close agreement with reference values obtained from the NIST Web book, and clearly captures the bulk condensation process above 40 bar.

Initial material characterisation

Preliminary T_2 relaxation measurements were performed on water saturated packed beds of each silica material; water provides a ubiquitous and easy to handle high proton density probe fluid which facilitates robust low-field NMR porosity and relaxation analysis under ambient conditions. **Figure 5** shows the resultant T_2 distributions, with each data set clearly exhibiting two separated T_2 populations. Following **Equation (3)** we may readily assign the populations at short T_2 to water confined within the silica mesopores, while the population at $T_2 \approx 2$ s is indicative of unrestricted water in the interparticle spaces; the small peak located at $T_2 \approx 0.9$ s is assigned to a small water population which exchanges between these environments on the time scale of the T_2 measurement.

Taking the Q6 material, wherein the very large S/V ratio (**Table 1**) of the silica makes the assumption $1 - P/T_{2,bulk} \ll P/T_{2,ads}$ most valid, a simple rearrangement of **Equation (3)** into the form

$$\rho_2 \approx \frac{V}{S}\frac{1}{T_2}, \tag{12}$$

combined with the assumption of spherical pores of diameter $d = 6V/S$, gives $\rho_2 \approx 0.125$ µm s^{-1}. This value is consistent with transverse surface relaxivity values obtained from high-purity colloidally-templated silicas in the absence of appreciable paramagnetic surface impurities ($\rho_2 = 0.122 - 0.203$ µm s^{-1})[87], in turn implying that surface-enhanced nuclear spin relaxation occurs within these materials as a result of reduced molecular mobility upon adsorption rather than via interactions within surface-bound paramagnetic species[88].

Total porosity values for these packed beds were obtained by comparing the acquired NMR signal magnitude to that from a known volume of water; these values are given in **Table 2** and are assumed relevant to the packed silica beds employed in our ethane measurements. **Table 2** further provides the percentage of intra-porosity found within the silica mesopores and the inter-porosity within the interparticle spaces; these values are obtained by integrating the two T_2 populations shown in **Figure 5**, where we assume the contribution of the exchange peak is negligible.

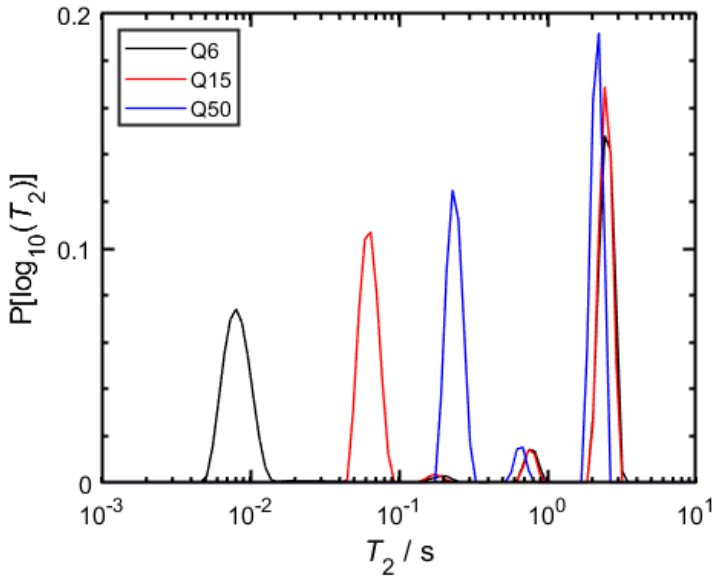

Figure 5. T_2 relaxation distributions obtained from water saturated packed beds of mesoporous Q-silicas. Two major T_2 populations are observed in each case, associated with confined water within the intraparticle mesopores (short T_2 values) and bulk-like water in the interparticle spaces (long T_2 values). A small but consistent population is also observed at an intermediate T_2 values and is assigned to water exchanging between these two environments on the time scale of the relaxation measurement.

Table 2. Silica bed porosity data obtained from NMR measurements of water saturated samples. Intraparticle and interparticle porosity values represent the percentage of the total porosity found within the intraparticle mesopores and interparticle spaces, respectively.

	Total porosity (ϕ)	Intraparticle porosity / %	Interparticle porosity / %
Q6	0.73	47	53
Q15	0.82	48	52
Q50	0.82	46	54

NMR ethane adsorption measurements

In analogy to our measurements of bulk ethane, the NMR signal associated with ethane in the presence of mesoporous silicas was approximated from the magnitude of the first echo of each acquired CPMG echo train. **Figure 6** reports the NMR-observed ethane content of our systems as a function of pressure, providing a comparison between bulk ethane and the ethane density in the cell when in the presence of our three mesoporous adsorbates. A clear step-change in ethane density is observed for all systems, again indicating ethane condensation at increased pressures. In systems containing the three mesoporous silicas this increase is observed within the pressure range 39 – 40 bar; these pressures are marginally lower than the condensation pressure observed for bulk ethane (40.1 – 40.8 bar), initially suggesting that capillary condensation processes may occur within the mesoporous structures of the silica particles, while bulk-like condensation is expected within the interparticle voids. However, fully reversible isotherms are observed across all three silica materials, which are not expected in the case of capillary condensation[89]; a possible explanation for the lack of observed hysteresis is as follows. Capillary condensation processes are expected to occur first within the smallest pore spaces present (pore throats) during the adsorption process. During desorption, these regions remain blocked as the liquid within these regions is the last to evaporate, leading to delayed desorption and hence hysteresis. However, the width of the resultant hysteresis loop is known to shrink with increasing temperature (and hence decreasing fluid surface tension) until the overlap of adsorption and desorption branches occurs at a critical temperature[90]. In the present work the experimental temperature employed (23.6 °C) is close to the critical temperature of ethane (32.18 °C) due to the limited working environment of our NMR equipment. Simple calculations utilising the Kelvin equation shown in **Equation (1)** (see **Supplementary Information**) reveal estimates of the anticipated ethane capillary condensation pressures in this study to be in the range 40.34 – 41.32 bar, 40.54 – 40.93 bar and 40.64 – 40.75 bar for the Q6, Q15 and Q50 materials, respectively, which take into account a spectrum of surface wetting behaviours. These narrow ranges incorporate the bulk saturated pressure of 40.68 bar at our experimental temperature, indicating that the detection of capillary condensation processes within our system is unlikely.

Figure 6 illustrates that at conditions where the bulk liquid is stable, the ethane density is greater than at the corresponding conditions in the systems containing porous silica; this observation is consistent with the occupation of cell space by the solid silica matrix. The near identical ethane density values observed within the Q15 and Q50 beds under liquid ethane conditions are consistent with the NMR porosity values detailed within **Table 2**, wherein the two beds are characterised by porosities of approximately 82 %. The clear decrease in ethane density within the Q6 bed, relative to the Q15 and Q50 systems, is further consistent with the porosity data in **Table 2**, which shows that the Q6 system exhibits a reduced porosity of 73 %. Under gas phase conditions the ethane density within the Q6 and Q15 systems is noticeably larger than is measured for the Q50 or bulk ethane systems, which we attribute to a consequence of significant adsorption within these

high surface area-to-volume ratio materials. As adsorption will also occur within the Q50 system we propose that the overlap of Q50 and bulk ethane density data at low pressures results from the cancellation of adsorption phenomena by the excluded volume of the solid matrix.

To further probe the capacity of our NMR measurements to probe ethane adsorption phenomena, we show in **Figure 7** a direct comparison of our NMR data with gravimetric adsorption measurements, performed under identical conditions; these data are limited to the pressure range of (25 to 39) bar to avoid the liquefaction phenomena demonstrated in **Figure 6**. For each data set shown in **Figure 7**, the excess NMR signal attributed to adsorption S_{ads} was calculated according to

$$S_{ads} = S_{exp} - S_{calc}. \tag{13}$$

Here S_{exp} is the experimentally measured NMR signal acquired for each mesoporous silica system at each pressure, while S_{calc} is the anticipated signal arising from the contribution of purely bulk ethane at each of these pressures, calculated according to

$$S_{calc} = \frac{\rho V \phi}{\alpha}. \tag{14}$$

Here ρ is the pressure-dependent bulk ethane density calculated using the reference equation of state implemented in the NIST database[86], V is the volume of the PEEK cell employed in the NMR measurements, ϕ is the total porosity of each silica packed bed given in **Table 2**, and α is the scaling factor between ethane quantity and NMR signal established in **Figure 4a**. The adsorption excess is then calculated as

$$q_{ex} = \frac{\alpha\, S_{ads}}{m_s}, \tag{15}$$

where m_s is the mass of mesoporous silica employed in each measurement.

Excellent agreement is apparent between our NMR and gravimetric adsorption data across both the Q6 and Q50 silica materials, with a maximum deviation of less than 0.2 mmol g^{-1} (approximately 5% of the observed ethane capacity) between the two measurements. Comparable agreement is also observed in the case of Q15 up to pressures of approximately 36 bar, beyond which the two data series diverge. While the source of this discrepancy is the subject of further investigation, the data within **Figure 7** provide a clear demonstration that low-field NMR analysis may be exploited to obtain quantitative hydrocarbon adsorption data from the interaction of mesoporous sorbents and gas phase hydrocarbons. The general trend of increasing adsorption capacity in the order Q6 > Q15 > Q50 is readily rationalised based on the surface-to-volume ratios of these materials (**Table 1**), with the largest such ratio corresponding to the greatest mass-based adsorption capacity in the presence of gaseous ethane.

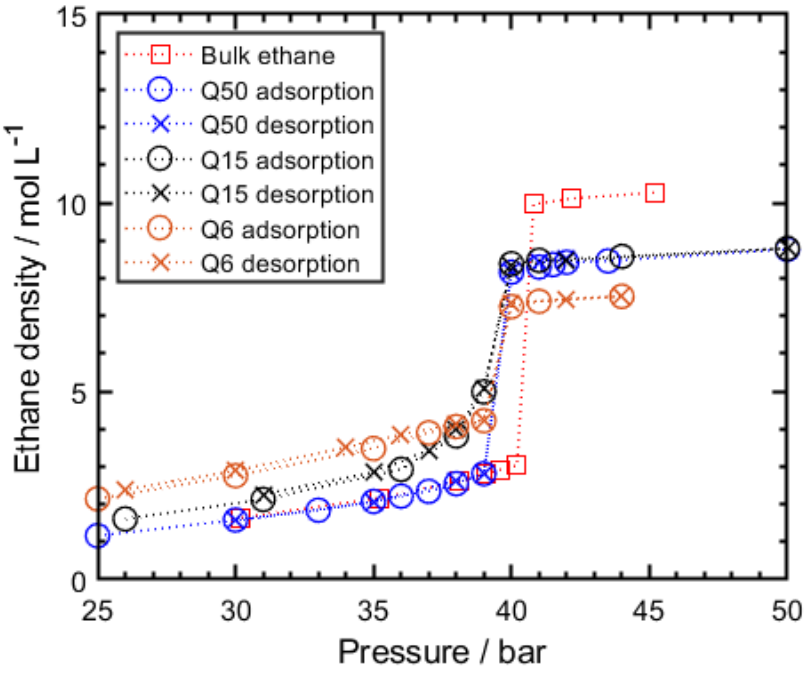

Figure 6. Calibrated NMR signal isotherms for ethane in the mesoporous silicas Q6, Q15 and Q50, as compared to the bulk fluid. Fully reversible isotherms are seen across all silica materials.

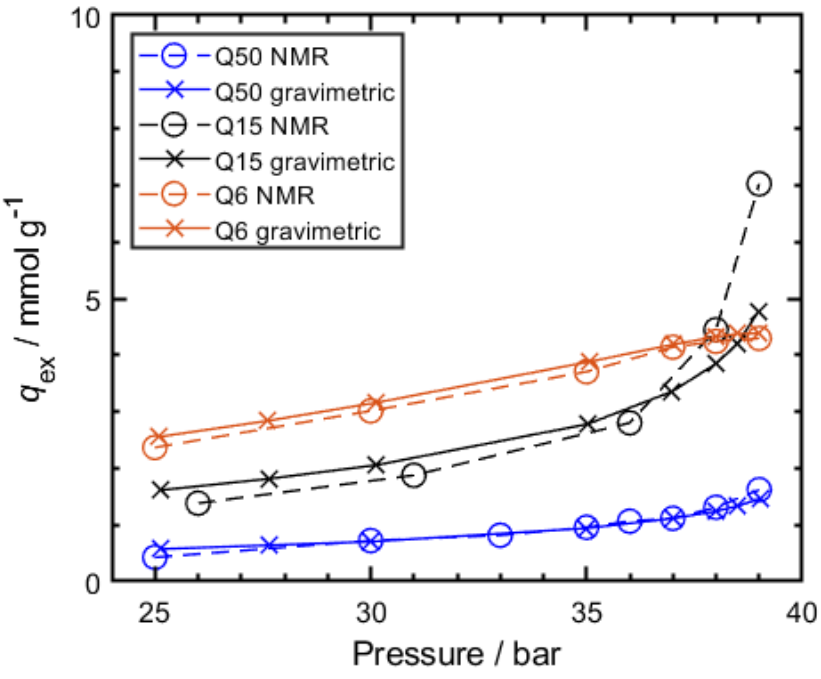

Figure 7. Direct comparison of the excess gas phase ethane adsorption capacities q_{ex} obtained via NMR and gravimetric measurements at pressures between 25 bar and 39 bar.

To demonstrate the capacity of NMR relaxation measurements for probing ethane adsorption phenomena, we show in **Figure 8a** an example series of T_2 distributions, characterising the pressure dependent relaxation behaviour of ethane within the Q15 silica bed. Two relaxation populations are clearly apparent at each pressure. For the distribution data obtained at pressures in excess of 40 bar these populations are readily assigned to liquid ethane within the intrapore and interpore spaces of the packed bed; in analogy to our preliminary water saturated measurements this assignment is based on the magnitude of the measured T_2 values, with the population exhibiting shorter T_2 values attributed to ethane confined within the intraparticle mesopores of the silica material. Further consistency with our saturated water data is also obtained when considering the integrated signal intensities of each population. For both the 41 bar and 44 bar data sets shown in **Figure 8a** such integration suggests 56 % of the ethane lies in the interparticle space, while 43 % is confined within the intraparticle mesopores; these values are in good agreement with porosity data shown in **Table 2**, which suggest these values to be 53 % and 47 %, respectively.

Assignment of the observed relaxation behaviour below the bulk condensation pressure is more complex. **Figure 8b** demonstrates the integrated signal intensities of the two observed T_2 populations as a function of pressure; for completeness, we note that this data is sensitive to both ethane within the adsorbed surface layer, as well as ethane away from the pore walls, and is therefore characteristic of the total ethane capacity q_t, rather than the excess quantities discussed above in relation to **Figure 7**. While we might expect the associated gas phase T_2 populations to follow the trend exhibited by the liquid phase, with shortened T_2 values indicating more confined species, this is not in fact the case for the integrated signal intensities of these populations. Rather, **Figure 8b** shows that the integrated population at short T_2 (~1 s or below) remains essentially constant as a function of increasing pressure, while the population at longer T_2 shows a clear increase in intensity; we interpret this behaviour as an indication of adsorption. Given the vast majority of ethane adsorption is anticipated to occur with the high surface area-to-volume ratio mesopores of the Q15 silica material, we therefore assign the population at increased T_2 to ethane within the intraparticle Q15 mesopores.

Our unconventional T_2 population assignment is supported via supplementary diffusion data presented in **Figure 8c**, which illustrates distributions of the observed ethane diffusion coefficients. Two separate diffusive populations are apparent at pressures below the bulk ethane condensation pressure; a rapidly diffusing population characterised by an essentially pressure invariant diffusion coefficient of $D \approx 2 \times 10^{-7}$ m^2 s^{-1}, together with a slower diffusing population with $D < 1 \times 10^{-7}$ m^2 s^{-1}. Following **Equation (5)** we may readily assign the signal population with the slowest diffusion coefficient to ethane within the intraparticle mesopore network, wherein repeated encounters with the pore walls facilitate the observation of effective self-diffusion, the rate of which is reduced from that of the unrestricted bulk fluid by the tortuosity of the mesopore network. In contrast, the more rapid diffusion coefficient is in fair agreement with the diffusive behaviour of bulk ethane

(observed to be between 2.5×10^{-7} m^2 s^{-1} and 1.5×10^{-7} m^2 s^{-1} at 23.6 °C and pressures between 30 bar and 39 bar) and is therefore assigned to ethane within the large interparticle spaces. The integrated populations of these two components are shown in **Figure 8d**, where a clear and significant increase in the population of the slower diffusing environment is evident with increasing pressure; we again interpret this increase as an indication of adsorption phenomena. A direct correlation between the relaxation and diffusion populations attributed to ethane within the intraparticle mesopores is provided in **Figure 8e**, revealing clear consistency between the two data sets, and providing validation for our peak assignments within **Figure 8a**.

The observation of rapid T_2 relaxation phenomena within the interparticle spaces of the Q15 packed bed may be rationalised based on the large diffusive distances that bulk-like ethane will cover during our NMR relaxation measurements. Detailed modelling has elucidated the occurrence of multiple magnetisation environments within the large interparticle pores prevalent to packed beds of spherical particles[91]. The somewhat exotic local magnetisation behaviour of such interparticle pore systems is attributed to differences in magnetic susceptibility between the solid and fluid materials under investigation[17]. Even under the conditions of the low static magnetic field strength employed here, extensive diffusion of proton bearing species through such varying fields is expected to facilitate an additional source of transverse nuclear spin relaxation, leading to a reduction in observed T_2 times below that expected from surface interactions alone. The realisation that such phenomena can potentially invert the expected T_2 magnitudes observed from pore structures of substantially different size is significant regarding future materials characterisation using hydrocarbon gas relaxation, and highlights the care needed to avoid of erroneous relaxation population assignment within hierarchically porous systems.

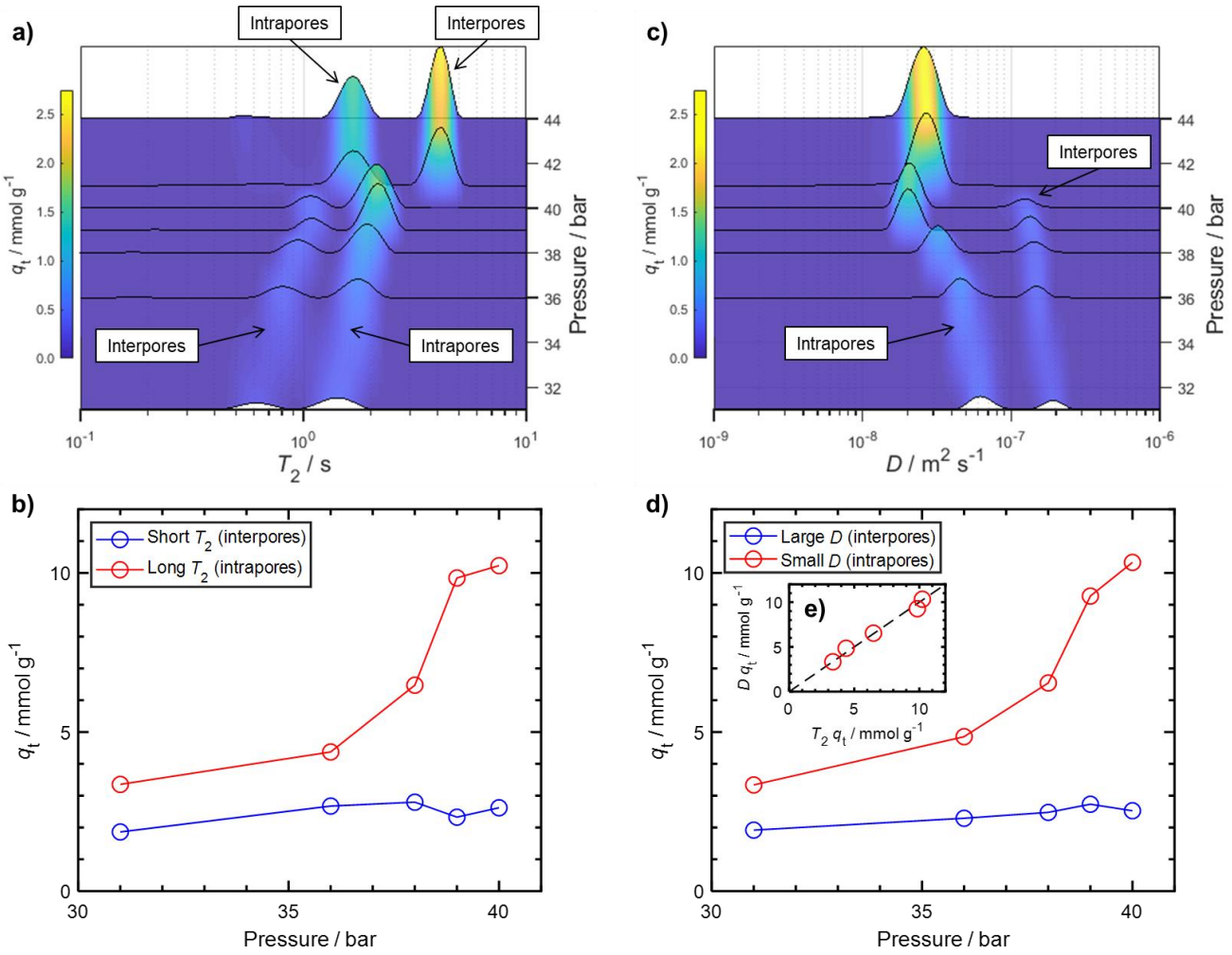

Figure 8. **a** T_2 distributions acquired from ethane in a packed bed of Q15 silica (approximately 4mm diameter spherical particles with 15 nm diameter pores) as a function of pressure between 31 bar and 44 bar. Within the liquid phase (> 40 bar) the population at short T_2 is assigned to ethane confined within the mesopores, while the population at longer T_2 is attributed to ethane within the interparticle space. **b** Integrated NMR signal intensities for the two T_2 populations present within the gas phase (pressure < 40 bar) from panel **a**, identified in terms of long (generally T_2 > 1 s) and short (generally T_2 < 1 s) T_2 relaxation characteristics. The large increase in ethane capacity with increasing pressure demonstrated at long T_2 is characteristic of the large surface area-to-volume ratio of intraparticle mesopores. **c** Self-diffusion coefficient (D) distributions from the same Q15 system as in panel **a**. The gas phase population with small D ($< 1 \times 10^{-7}$ m^2 s^{-1}) is assigned to ethane within the intraparticle Q15 pore space based on the expected reduction in molecular mobility within the tortuous mesoporous network; the large D ($> 1 \times 10^{-7}$ m^2 s^{-1}) of the second population is close to that of the unrestricted bulk, characteristic of ethane within the interparticle spaces. **d** Integrated NMR signal intensities from the two diffusion populations present within the gas phase (pressure < 40 bar) from panel **c**, identified in terms of large and small D Values. **e** Direct comparison between relaxation and diffusion derived absolute intraparticle gas phase ethane capacities, demonstrating excellent agreement.

5. Conclusions

In this work we have explored a series of low-field NMR measurements to examine ethane behaviour within packed beds of mesoporous silica materials exhibiting pore sizes between 6 and 50 nm. This investigation has demonstrated the clear utility of such measurements in obtaining quantitative ethane uptake data at pressures up to the bulk condensation point. Excellent agreement is observed through a direct comparison of NMR calculated excess adsorption capacities and gravimetric adsorption measurements. NMR T_2 relaxation distribution data has further been demonstrated as a facile approach with which to quantify and contrast the absolute adsorption capacities of intraparticle mesopores against interparticle voids, with the assignment of differing relaxation phenomena to ethane within distinctly different pore structures validated through the acquisition of PFG NMR diffusion data. Overall, our results highlight benchtop NMR as a potentially useful tool in the screening of short chain hydrocarbon adsorption phenomena within porous materials of relevance to gas processing and catalytic transformations without the need for specialist sorption hardware.

Acknowledgements

PhD financial support from the China Scholarship Council (No. 201708190001) for Kaishuo Yang is gratefully acknowledged. Funding from the ARC (Linkage grant LP180100116) is also gratefully acknowledged.

References

[1] J. Rouquerol, F. Rouquerol, P. Llewellyn, G. Maurin, K. S. W. Sing, *Adsorption by Powders and Porous Solids: Principles, Methodology and Applications: Second Edition*, Elsevier Inc., **2013**.

[2] Z. Li, S. Das, P. Hongmanorom, N. Dewangan, M. H. Wai, S. Kawi, *Catal. Sci. Technol.* **2018**, *8*, 2763–2778.

[3] M. Oschatz, J. P. Hofmann, T. W. van Deelen, W. S. Lamme, N. A. Krans, E. J. M. Hensen, K. P. de Jong, *ChemCatChem* **2017**, *9*, 620–628.

[4] W. S. Chiang, E. Fratini, P. Baglioni, J. H. Chen, Y. Liu, *Langmuir* **2016**, *32*, 8849–8857.

[5] Y. Ren, Z. Ma, P. G. Bruce, *Chem. Soc. Rev.* **2012**, *41*, 4909–4927.

[6] A. Cybula, M. Klein, A. Zaleska, *Appl. Catal. B Environ.* **2015**, *164*, 433–442.

[7] M. Haneda, E. Joubert, J.-C. Ménézo, D. Duprez, J. Barbier, N. Bion, M. Daturi, J. Saussey, J.-C. Lavalley, H. Hamada, *Phys. Chem. Chem. Phys.* **2001**, *3*, 1366–1370.

[8] M. Saito, T. Aihara, H. Miura, T. Shishido, *Catal. Today* **2021**, *375*, 64–69.

[9] D. Dutta, S. Chatterjee, K. T. Pillai, P. K. Pujari, B. N. Ganguly, *Chem. Phys.* **2005**, *312*, 319–324.

[10] E. D. E. R. Hyde, A. Seyfaee, F. Neville, R. Moreno-Atanasio, *Ind. Eng. Chem. Res.* **2016**, *55*, 8891–8913.

[11] A. Berggren, A. E. C. Palmqvist, K. Holmberg, *Soft Matter* **2005**, *1*, 219–226.

[12] J.-H. Yun, T. Düren, F. J. Keil, N. A. Seaton, *Langmuir* **2002**, *18*, 2693–2701.

[13] G. C. Watson, N. K. Jensen, T. E. Rufford, K. I. Chan, E. F. May, *J. Chem. Eng. Data* **2011**, *57*, 93–101.

[14] T. Wu, H. Zhao, S. Tesson, A. Firoozabadi, *Fuel* **2019**, *235*, 855–867.

[15] M. Thommes, K. Kaneko, A. V. Neimark, J. P. Olivier, F. Rodriguez-Reinoso, J. Rouquerol, K. S. W. Sing, *Pure Appl. Chem.* **2015**, *87*, 1051–1069.

[16] C. Terenzi, A. J. Sederman, M. D. Mantle, L. F. Gladden, *J. Phys. Chem. Lett.* **2019**, *10*, 5781–5785.

[17] J. Mitchell, T. C. Chandrasekera, M. L. Johns, L. F. Gladden, E. J. Fordham, *Phys. Rev. E* **2010**, *81*, 026101.

[18] J. Kowalewski, L. Mäler, *Nuclear Spin Relaxation in Liquids: Theory, Experiments, and Applications*, CRC Press, **2017**.

[19] B. E. Kinn, T. R. Myers, A. M. Allgeier, *Curr. Opin. Chem. Eng.* **2019**, *24*, 115–121.

[20] J.-P. Korb, *Prog. Nucl. Magn. Reson. Spectrosc.* **2018**, *104*, 12–55.

[21] E. V. Silletta, M. B. Franzoni, G. A. Monti, R. H. Acosta, *Microporous Mesoporous Mater.* **2018**, *269*, 17–20.

[22] S. Davies, K. J. Packer, *J. Appl. Phys.* **1990**, *67*, 3163–3170.

[23] J. Mitchell, J. D. Griffith, J. H. P. Collins, A. J. Sederman, L. F. Gladden, M. L. Johns, *J. Chem. Phys.* **2007**, *127*, 234701.

[24] K. E. Washburn, P. T. Callaghan, *Phys. Rev. Lett.* **2006**, *97*, 175502.

[25] M. A. Isaacs, C. M. A. Parlett, N. Robinson, L. J. Durndell, J. C. Manayil, S. K. Beaumont, S. Jiang, N. S. Hondow, A. C. Lamb, D. Jampaiah, M. L. Johns, K. Wilson, A. F. Lee, *Nat. Catal.* **2020**, *3*, 921–931.

[26] J. J. Chen, X. Kong, K. Sumida, M. A. Manumpil, J. R. Long, J. A. Reimer, *Angew. Chemie - Int. Ed.* **2013**, *52*, 12043–12046.

[27] J. J. Chen, J. A. Mason, E. D. Bloch, D. Gygi, J. R. Long, J. A. Reimer, *Microporous Mesoporous Mater.* **2015**, *205*, 65–69.

[28] V. J. Witherspoon, L. M. Yu, S. Jawahery, E. Braun, S. M. Moosavi, S. K. Schnell, B. Smit, J. A. Reimer, *J. Phys. Chem. C* **2017**, *121*, 15456–15462.

[29] J. -P. Korb, S. Xu, J. Jonas, *J. Chem. Phys.* **1993**, *98*, 2411–2422.

[30] J. -P. Korb, A. Delville, S. Xu, G. Demeulenaere, P. Costa, J. Jonas, *J. Chem. Phys.* **1994**, *101*, 7074–7081.

[31] D. Weber, J. Mitchell, J. Mcgregor, L. F. Gladden, *J. Phys. Chem. C* **2009**, *113*, 6610–6615.

[32] C. D'Agostino, J. Mitchell, M. D. Mantle, L. F. Gladden, *Chem. - A Eur. J.* **2014**, *20*, 13009–13015.

[33] N. Robinson, C. Robertson, L. F. Gladden, S. J. Jenkins, C. D'Agostino, *ChemPhysChem* **2018**, *19*, 2472–2479.

[34] N. Robinson, P. Bräuer, A. York, C. D'Agostino, *Phys. Chem. Chem. Phys.* **2021**, *23*, 17752-17760.

[35] J. Ward-Williams, L. F. Gladden, *Magn. Reson. Imaging* **2019**, *56*, 57–62.

[36] J. Ward-Williams, J. P. Korb, L. F. Gladden, *J. Phys. Chem. C* **2018**, *122*, 20271–20278.

[37] J. Ward-Williams, J.-P. Korb, L. Rozing, A. J. Sederman, M. D. Mantle, L. F. Gladden, *J. Phys. Chem. C* **2021**, *125*, 8767–8778.

[38] A. Papaioannou, R. Kausik, *Phys. Rev. Appl.* **2015**, *4*, 024018.

[39] W. S. Price, *Concepts Magn. Reson.* **1997**, *9*, 299–336.

[40] J. Kärger, M. Avramovska, D. Freude, J. Haase, S. Hwang, R. Valiullin, *Adsorption* **2021**, *27*, 453–484.

[41] D. Weber, A. J. Sederman, M. D. Mantle, J. Mitchell, L. F. Gladden, *Phys. Chem. Chem. Phys.* **2010**, *12*, 2619–2624.

[42] N. Robinson, C. D'Agostino, *Top. Catal.* **2020**, *63*, 319–327.

[43] M. Dvoyashkin, A. Khokhlov, S. Naumov, R. Valiullin, *Microporous Mesoporous Mater.* **2009**, *125*, 58–62.

[44] T. J. Rottreau, C. M. A. Parlett, A. F. Lee, R. Evans, *J. Phys. Chem. C* **2017**, *121*, 16250–16256.

[45] C. D'Agostino, J. Mitchell, L. F. Gladden, M. D. Mantle, *J. Phys. Chem. C* **2012**, *116*, 8975–8982.

[46] M. A. Isaacs, N. Robinson, B. Barbero, L. J. Durndell, J. C. Manayil, C. M. A. Parlett, C. D'Agostino, K. Wilson, A. F. Lee, *J. Mater. Chem. A* **2019**, *7*, 11814–11825.

[47] F. Stallmach, J. Kärger, C. Krause, M. Jeschke, U. Oberhagemann, *J. Am. Chem. Soc.* **2000**, *122*, 9237–9242.

[48] S. Naumov, R. Valiullin, J. Kärger, R. Pitchumani, M. O. Coppens, *Microporous Mesoporous Mater.* **2008**, *110*, 37–40.

[49] D. Kondrashova, A. Lauerer, D. Mehlhorn, H. Jobic, A. Feldhoff, M. Thommes, D. Chakraborty, C. Gommes, J. Zecevic, P. de Jongh, A. Bunde, J. Kärger, R. Valiullin, *Sci. Reports* **2017**, *7*, 1–10.

[50] Y. Hu, M. Li, G. Hou, S. Xu, K. Gong, X. Liu, X. Han, X. Pan, X. Bao, *Nano Res.* **2017**, *11*, 360–369.

[51] Y. Hu, X. Pan, X. Han, X. Bao, *J. Phys. Chem. C* **2017**, *121*, 2481–2486.

[52] Y. Hu, Q. Zhang, M. Li, X. Pan, B. Fang, W. Zhuang, X. Han, X. Bao, *J. Phys. Chem. C* **2016**, *120*, 19885–19889.

[53] B. Blümich, *J. Magn. Reson.* **2019**, *306*, 27–35.

[54] J. Mitchell, L. F. Gladden, T. C. Chandrasekera, E. J. Fordham, *Prog. Nucl. Magn. Reson. Spectrosc.* **2014**, *76*, 1–60.

[55] M. L. Johns, E. O. Fridjonsson, S. J. Vogt, A. Haber, Eds. , *Mobile NMR and MRI: Developments and Applications*, Royal Society Of Chemistry, Cambridge, **2015**.

[56] Y. Tang, D. McCowan, Y. Q. Song, *Sci. Rep.* **2019**, *9*, 11174.

[57] A. Duchowny, P. M. Dupuy, H. C. Widerøe, O. J. Berg, A. Faanes, A. Paulsen, H. Thern, O. Mohnke, M. Küppers, B. Blümich, A. Adams, *J. Magn. Reson.* **2021**, *329*, 107025.

[58] J. D. Kerr, B. J. Balcom, M. J. McCarthy, M. P. Augustine, *J. Magn. Reson.* **2019**, *304*, 35–41.

[59] C. Horch, S. Schlayer, F. Stallmach, *J. Magn. Reson.* **2014**, *240*, 24–33.

[60] H. Thern, C. Horch, F. Stallmach, B. Li, A. Mezzatesta, H. Zhang, R. Arro, *Microporous Mesoporous Mater.* **2018**, *269*, 21–25.

[61] N. Robinson, G. Xiao, P. R. J. Connolly, N. N. A. Ling, E. O. Fridjonsson, E. F. May, M. L. Johns, *Phys. Chem. Chem. Phys.* **2020**, *22*, 13689–13697.

[62] J. Marreiros, R. de Oliveira-Silva, P. Iacomi, P. L. Llewellyn, R. Ameloot, D. Sakellariou, *J. Am. Chem. Soc.* **2021**, *143*, 8249–8254.

[63] K. W. Kolasinski, *Surface Science: Foundations of Catalysis and Nanoscience*, Wiley, Hoboken, NJ, USA, **2020**.

[64] L. R. Fisher, J. N. Israelachvili, *Nature* **1979**, *277*, 548–549.

[65] W. Thomson, *Proc. R. Soc. Edinburgh* **1872**, *7*, 63–68.

[66] A. C. Mitropoulos, *J. Colloid Interface Sci.* **2008**, *317*, 643–648.

[67] Y. Zhang, G. J. Hirasaki, W. V. House, R. Kobayashi, in *SPWLA Annu. Logging Symp.*, OnePetro, **2002**, p. SPWLA-2002-HHH.

[68] P. M. Singer, D. Asthagiri, W. G. Chapman, G. J. Hirasaki, *J. Chem. Phys.* **2018**, *148*, 204504.

[69] P. S. Hubbard, *Phys. Rev.* **1963**, *131*, 1155–1165.

[70] Y.-Q. Song, R. Kausik, *Prog. Nucl. Magn. Reson. Spectrosc.* **2019**, *112–113*, 17–33.

[71] Y. Q. Song, *J. Magn. Reson.* **2013**, *229*, 12–24.

[72] W. S. Price, *NMR Studies of Translational Motion*, Cambridge University Press, **2009**.

[73] H. Y. Carr, E. M. Purcell, *Phys. Rev.* **1954**, *94*, 630–638.

[74] S. Meiboom, D. Gill, *Rev. Sci. Instrum.* **1958**, *29*, 688–691.

[75] E. O. Stejskal, J. E. Tanner, *J. Chem. Phys.* **1965**, *42*, 288–292.

[76] J. E. Tanner, *J. Chem. Phys.* **1970**, *52*, 2523–2526.

[77] J. D. Wilson, *J. Mater. Sci.* **1992**, *27*, 3911–3924.

[78] E. O. Stejskal, J. E. Tanner, *J. Chem. Phys.* **1965**, *42*, 288–292.

[79] A. N. Tikhonov, V. I. A. Arsenin, *Solutions of Ill-Posed Problems*, SIAM, **1977**.

[80] G. H. Golub, M. Heath, G. Wahba, *Technometrics* **1979**, *21*, 215–223.

[81] J. D. Griffith, A. E. Bayly, M. L. Johns, *J. Colloid Interface Sci.* **2007**, *315*, 223–229.

[82] K. G. Hollingsworth, M. L. Johns, *J. Colloid Interface Sci.* **2003**, *258*, 383–389.

[83] R. Kleinrahm, X. Yang, M. O. McLinden, M. Richter, *Adsorpt.* **2019**, *25*, 717–735.

[84] X. Yang, R. Kleinrahm, M. O. McLinden, M. Richter, *Adsorpt.* **2020**, *26*, 645–659.

[85] D. Bücker, W. Wagner, *J. Phys. Chem. Ref. Data* **2006**, *35*, 205.

[86] "NIST Chemistry WebBook," can be found under https://webbook.nist.gov/chemistry/

[87] A. T. Krzyżak, I. Habina, *Microporous Mesoporous Mater.* **2016**, *231*, 230–239.

[88] L. F. Gladden, J. Mitchell, *New J. Phys.* **2011**, *13*, 035001.

[89] E. Barsotti, S. P. Tan, M. Piri, J. H. Chen, *Fuel* **2020**, *263*, 116441.

[90] E. Barsotti, S. P. Tan, M. Piri, J.-H. Chen, *Langmuir* **2018**, *34*, 4473–4483.

[91] J. Mitchell, E. Fordham, *Phys. Rev. Mater.* **2019**, *3*, 055604.